ACS APPLIED ENERGY MATERIALS

www.acsaem.org Article

Complex Structure of Molten NaCl–$CrCl_3$ Salt: Cr–Cl Octahedral Network and Intermediate-Range Order

Qing-Jie Li, David Sprouster, Guiqiu Zheng, Jörg C. Neuefeind, Alexander D. Braatz, Joanna Mcfarlane, Daniel Olds, Stephen Lam, Ju Li,* and Boris Khaykovich*

Cite This: *ACS Appl. Energy Mater.* 2021, 4, 3044–3056 Read Online

ACCESS | Metrics & More | Article Recommendations

ABSTRACT: The resurgence of the molten-salt nuclear reactors (MSRs) creates interesting problems in molten-salt chemistry. As MSRs operate, the composition and physical properties of salts change because of fission and corrosion. Since Cr is the principal corrosion product and NaCl is a common constituent, we studied the atomic structure of molten NaCl–$CrCl_3$. We found networks of $CrCl_6^{3-}$ octahedra and an intermediate-range order with a non-monotonic temperature behavior with a remarkable agreement between measurements and *ab initio* simulations. Even though the corrosion results in minute quantities of dissolved Cr, the speciation of Cr could lead to changes in molten-salt properties in nuclear and solar salts. In particular, we found a much lower melting temperature than expected and a broad metastable liquid–solid coexistence phase. The availability of Cr isotopes with very different neutron scattering properties makes Cr an ideal model multivalent ion for experimental validation of new atomistic models such as neural network interatomic potentials.

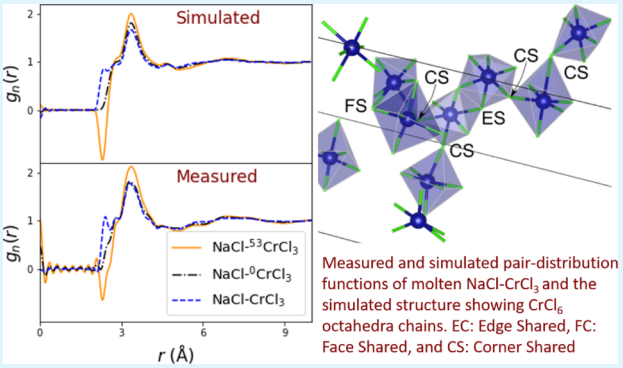

Measured and simulated pair-distribution functions of molten NaCl-$CrCl_3$ and the simulated structure showing $CrCl_6$ octahedra chains. EC: Edge Shared, FC: Face Shared, and CS: Corner Shared

KEYWORDS: *molten salt, pair distribution function, phase diagram, melting, prepeak, chromium chloride, sodium chloride*

1. INTRODUCTION

Molten-salt nuclear reactor (MSR) concepts are important candidates for next-generation nuclear power reactors, which promise to be safer and more efficient than existing water-based ones.[1,2] Molten salts for MSRs are divided into two broad classes: coolant salts and fuel salts. While coolant salts are used to remove the heat generated by nuclear reactions, fuel salts contain dissolved nuclear fuel. As the MSRs operate, chemical compositions of both salts change. Nuclear fuel burning creates new chemical species in fuel salts (fission, transmutation, and decay products), while the composition of coolant salts experiences effects of corrosion and radiolysis, leading to changes in key physical properties of the melts such as density, diffusivity, viscosity, thermal capacity, and so on (corrosion is important for other applications of molten salts, such as in solar thermal energy and heat storage). The design of fully functional MSRs requires predictive modeling of these changing physical properties. Successful modeling can only be done based on detailed knowledge of the molecular structure and speciation for the salt components and impurities.[1−3]

The microscopic structure of liquids is described by the pair distribution function (PDF), which measures the distribution of distances between atoms in the liquid phase.[4,5] For multicomponent mixtures, it is important to determine *partial* PDFs (correlations between particular kinds of ions) since interatomic potentials are different for different ionic species. Predictions of the partial PDFs can be made using both classical and *ab initio* molecular dynamics (MD) simulations, which are crucial for predicting changes in physical and chemical properties of molten salts.[1−3,6] However, the assumptions and approximations underlying these MD simulations must be carefully validated with experimental measurements since (1) the accuracy of physics-informed empirical interatomic potentials is often limited by the assumed functional form and (2) even *ab initio* MD simulations inevitably involve simplifying assumptions and approximations such as semi-empirical corrections for dispersion interactions, leading to potential disagreement with experimentally measured properties.[7,8] The situation is made more complicated by Coulomb interactions, which dominate short- and medium-range structures in molten salts.

Received: October 28, 2020
Accepted: February 23, 2021
Published: March 16, 2021

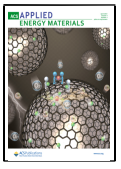

https://doi.org/10.1021/acsaem.0c02678
ACS Appl. Energy Mater. 2021, 4, 3044–3056

Recently, machine learning-based interatomic potentials have demonstrated huge potential for efficient yet accurate molten-salt modeling.[9,10] However, their accuracy is intrinsically bounded by the training data collected from *ab initio* MD simulations. Therefore, careful experimental measurements are needed to validate *ab initio* MD. Once validated, fast and accurate machine learning potentials could be prepared and used to predict thermodynamic and transport properties of the melts.[1−3,6] Since PDFs can be experimentally measured using neutron and X-ray diffraction, a direct comparison between experiments and simulations can be made. Here, we report a combined investigation of the structure of the molten NaCl−$CrCl_3$ near-eutectic mixture by the diffraction measurements and *ab initio* MD simulations.

We chose a NaCl−$CrCl_3$ near-eutectic mixture to elucidate the behavior of Cr ions, the most important corrosion product dissolved in the salts. These Cr ions come from structural metal alloys that are in contact with molten salts, for example, stainless-steel or high-nickel alloys.[11] Despite the wealth of recent corrosion studies and the importance of Cr as a corrosion product, the phase diagram of NaCl−$CrCl_3$ and similar mixtures has not received recent attention.[12−16] Moreover, to the best of our knowledge, the local structure of Cr-containing molten salts has not been measured before, although it has been analyzed by *ab initio* MD simulations in fluoride salts.[7] Furthermore, Cr ions can exist in various valence states in the melt, altering the redox potential of the salt, interacting with other salt components (U, Te, Mg, Ni, *etc.*) and adding complexity to the corrosion processes. Although corrosion generally results in relatively small quantities of Cr in the melt (tens of ppm[17,18]), the near-eutectic NaCl−$CrCl_3$ permits high-resolution measurements of the structure around Cr ions.

2. EXPERIMENTAL AND COMPUTATIONAL METHODS

2.1. Sample Preparation. We chose near-eutectic composition of 78% NaCl and 22% $CrCl_3$ (in mol %).[13] The molar concentration ratio is $c_{Na}/c_{Cr}/c_{Cl}$ = 0.32:0.09:0.59. This composition has a melting temperature of about 600 °C according to the published phase diagram.[13] We confirmed that the salt was completely molten above 600 °C, but our measurements showed a more complicated picture, as described below.

Samples of natural (non-isotopically substituted Cr) salts were prepared using commercially available high-purity NaCl and $CrCl_3$ (NaCl >99.5% and $CrCl_3$ >99%, Sigma-Aldrich). The salt powders were weighed, mixed, and melted in a glovebox filled with Ar. To ensure homogeneity, the mixed powders were remelted twice at 820 °C. To ensure that the composition of the salt did not change due to evaporation and sublimation during preparation, we measured the total mass of NaCl and $CrCl_3$ powders before melting and the mass of the prepared NaCl−$CrCl_3$ after melting. Figure 1 shows that the mass loss due to the heating is below 1%. Therefore, effects of the mass loss on the overall composition are minimal.

For neutron and X-ray diffraction measurements, the salt samples were loaded into quartz capillaries (standard thin-wall quartz NMR capillaries, 5 mm outer diameter for neutrons, 1 mm for X-rays, from Wilmad-LabGlass). The capillaries were flame-sealed under rough vacuum and allowed to cool in the glovebox furnace for testing the stability under thermal cycling.

Isotopically enriched compositions were prepared by chlorination of commercially available $^{53}Cr_2O_3$. Chromium(III) chloride is typically prepared by chlorination of chromium metal directly, by carbothermic chlorination of oxide at elevated temperature, or by the dissolution of chromium metal or chromium(III) oxide in hydrochloric acid. The isotopically enriched chromium was supplied as

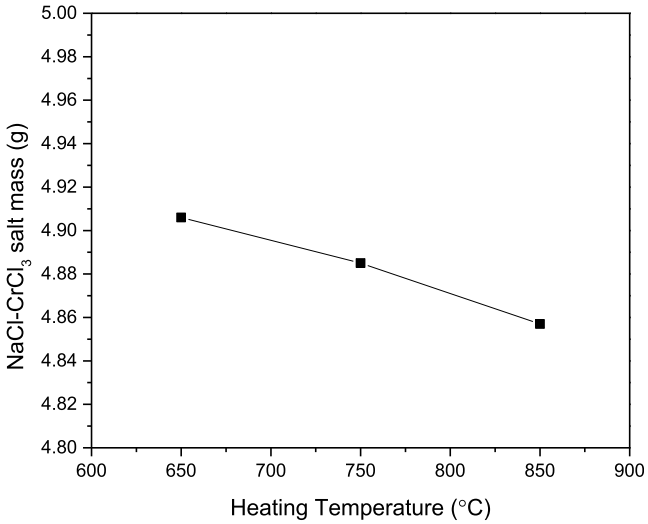

Figure 1. Mass change of NaCl−$CrCl_3$ salt after heating at different temperatures for 30 min.

chromium(III) oxide. With the need for anhydrous $CrCl_3$ and the oxide form supplied for this experiment, the carbothermic chlorination by carbon tetrachloride was chosen as the optimal pathway for conversion. The reaction for this conversion is as follows

$$Cr_2O_3 + 3CCl_4 \rightarrow 2CrCl_3 + 3COCl_2 \quad (1)$$

After purging for approximately 5 min, the furnace was turned on, set to 450 °C, and monitored with both the furnace and external thermocouple suspended on the outside of the quartz tube in the middle of the furnace. The tube and material equilibrated at 450 °C for approximately 10 min with a flowing at 0.2−0.3 SCFH before the furnace set point was increased to 800 °C and the gas flow rate decreased to 0.1−0.2 SCFH. After reaching 800 °C, the 3-way valve was switched to allow the argon flow to pass through a bubbler filled with 50 mL of carbon tetrachloride sitting in a water bath at approximately 50 °C. The furnace exhaust for this reaction is first routed through a chiller to return the gas to room temperature and then bubbled through a 1 M NaOH solution to remove phosgene safely before venting to the hood. After 2 h, the furnace was opened, and the quartz boat was visually inspected for residual oxide. If no oxide was present, the 3-way valve was switched to flow just Ar through the tube furnace and the flow rate was increased to remove any residual carbon tetrachloride from the flow path. The conversion to $CrCl_3$ forms dark purple, sheet-like crystals adhered to the upper portion of the quartz tube with no material remaining in the boat. The furnace was allowed to cool under argon flow to room temperature and all the fittings were removed. The $CrCl_3$ crystals were then removed toward the gas inlet side of the tube to avoid contamination of the crystals with white solids that formed from the breakdown of carbon tetrachloride at elevated temperatures. The crystals were then carefully weighed into a sample vial and stored for shipment or used for conversion to $CrCl_2$.

Approximately, 1 g of $^{53}Cr_2O_3$ was weighed into a quartz boat and spread evenly. The quartz boat was then inserted into the open end of a tube furnace and centered in the middle of the heated zone. The tube was then sealed and purged with argon gas to remove any residual air. A schematic for the setup used for the conversion is shown in Figure 2.

Within converted chromium chlorides, the concentration of ^{53}Cr was about 97% among four Cr isotopes (50, 52, 53, and 54). This concentration was measured using inductively coupled plasma mass spectroscopy (ICP−MS, 7900 system from Agilent Scientific Instrument). For ICP−MS, the converted isotopic chromium (II) chloride ($^{53}CrCl_2$) was completely dissolved and diluted in 2% HNO_3 solution. We found 97% of isotopic enrichment of ^{53}Cr with excellent repeatability.

https://doi.org/10.1021/acsaem.0c02678
ACS Appl. Energy Mater. 2021, 4, 3044−3056

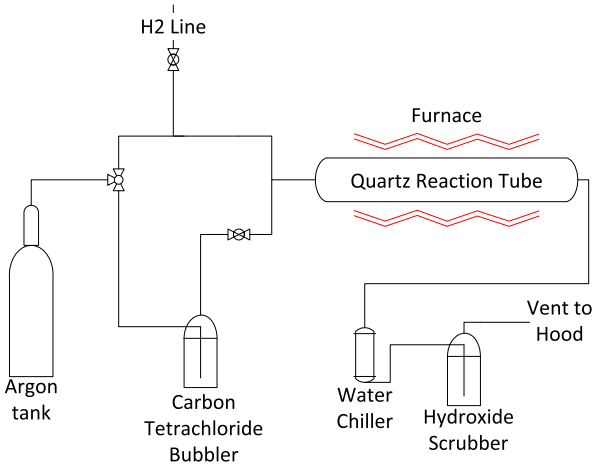

Figure 2. Design schematic for $CrCl_3$ production.

2.2. Neutron Diffraction Methods. Neutron diffraction measurements were conducted at NOMAD at the Spallation Neutron Source at Oak Ridge National Laboratory.[19] The scattered beam intensity was calibrated using vanadium and diamond standards. For heating the samples, we used a standard vanadium furnace routinely used at NOMAD. Vacuum-sealed quartz capillaries contained enough salt powder for up to 0.5 mL of melt. The cross-section of the incoming neutron beam was always slightly smaller than the cross-section of the melt such that the diffracted beam intensity could be directly compared with that of calibration standards. The detected neutron signal was normalized to the proton charge of the SNS proton-beam accelerator and corrected by a wavelength-dependent absorption factor. Using the known sample composition and tabulated neutron scattering cross-sections, the intensity was directly compared with the computer-simulated PDF.

2.3. X-ray Diffraction Methods. X-ray diffraction measurements were conducted at the XPDF beamline (28-ID-1) at the National Synchrotron Light Source II at Brookhaven National Laboratory. The quartz capillaries were resistively heated using a nichrome wire, and the temperature was measured using a standard thermocouple near the molten zone. All measurements were performed in the transmission mode with an amorphous silicon-based flat panel detector (PerkinElmer) mounted orthogonally to the beam path. The sample-to-detector distance and tilt of the detector relative to the beam were refined using a Ni powder standard. The wavelength of the incident X-rays was 0.1671 Å (74.21 keV) and the sample-to-detector distance was calculated to be 282.74 mm. All raw two-dimensional patterns were background-corrected by subtracting a dark current image. Noticeable artifact regions of the detector (beam stop and damaged pixels) were masked. The corrected and masked two-dimensional detector images were then radially integrated to obtain one-dimensional powder diffraction patterns. The background signal (quartz capillary and air scattering) was subtracted from the individual XRD patterns. The powder patterns were corrected for PDF-specific corrections (self-absorption, multiple scattering, and Compton scattering)[20] and converted to atomic PDFs, $G_X(r)$, using PDFgetX3[21] over a Q-range of 0.1−22.0 $Å^{-1}$. The atom positions for the molten phase generated from VASP[22−25] were imported into TOPAS software (Bruker), and an X-ray PDF pattern was forward predicted using a known instrument function for the XPDF beamline.

2.4. *Ab Initio* Molecular Dynamics Methods. *Ab initio* MD simulations were carried out using the Vienna *ab initio* simulation package (VASP)[22−25] under the Born-Oppenheimer approximation. For electronic self-consistent calculations, the generalized gradient approximation (GGA) in the form of Perdew−Burke−Ernzerhof (PBE)[26,27] was adopted for the exchange−correlation functional. Core electrons were modeled using projector-augmented wave (PAW) pseudo-potentials[28,29] (Na_pv: $2p^6 2s^1$, Cl: $3s^2 3p^5$, and Cr_pv: $3p^6 3d^5 s^1$) with an energy cutoff of 600 eV. We used Gaussian smearing with a width of 0.05 eV for partial occupancy of states and only the Γ point for Brillouin zone integration. Spin polarization was included to capture the magnetic properties of elemental Cr. Additionally, DFT-D2 van der Waals corrections from Grimme were employed to account for dispersion interactions.[30] The convergence criterion for self-consistent calculations was set to 0.1 meV. MD simulations were carried out in an isobaric−isothermal (*NPT*, *i.e.*, constant number of atoms N, pressure P, and temperature T) ensemble at 1 atm pressure. The supercell was first initialized with a random structure generated with the Packmol package to avoid overlapping atomic positions.[31] In total, the supercell contains 72 Cl atoms, 11 Cr atoms, and 39 Na atoms to represent the composition used in the measurements. The initial random configuration was equilibrated at 926.85 °C for 20 ps to develop the liquid structure. The equilibrated liquid structure was cooled to 701.85 °C, the temperature of the measurements, within another 20 ps. Finally, a ∼40 ps long equilibrium MD simulation was performed at 701.85 °C to calculate various liquid properties. According to previous work, a simulation time of 40 ps should be sufficient to obtain converged molten-salt properties.[32] A time step of 1 fs was used for all MD simulations. The time-averaged box lengths along x, y, and z directions are 17.3, 14.4, and 14.1 Å, respectively.

3. EXPERIMENTAL AND COMPUTATIONAL RESULTS

Our main result is shown in Figure 3. This figure shows total PDFs of isotopically substituted NaCl−$CrCl_3$. Isotopic substitution of ^{53}Cr does not change the chemistry and interatomic interactions that are determined mostly by outer electron shells. However, it changes the neutron scattering cross-section of Cr in a profound way.[33] The

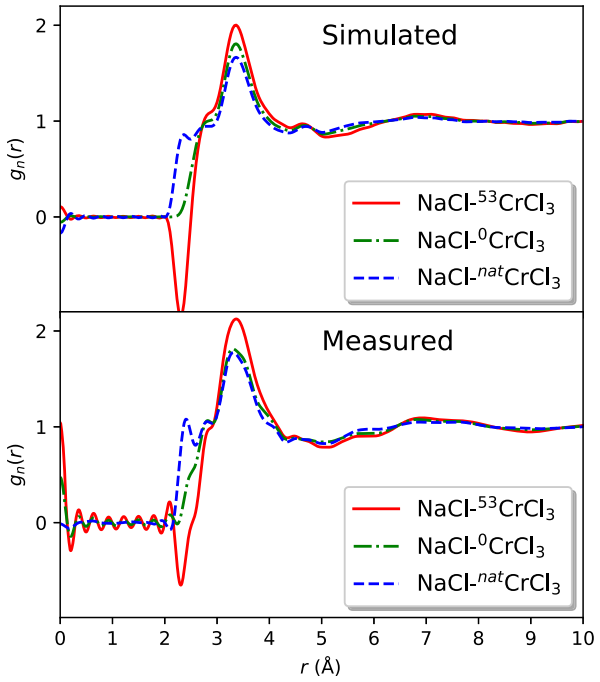

Figure 3. Simulated (top) and measured (bottom) PDFs (neutron) of three chemically identical molten NaCl−$CrCl_3$ mixtures with different isotopic contents of Cr: natural Cr, 100% ^{53}Cr, and the zero-mix (the mixture of isotopes that results in no neutron diffraction signal from Cr). These neutron diffraction measurements of the liquid phase were conducted at 700 °C. Simulations are time-averaged partial PDFs from AIMD simulations, namely, the weighted sum of the partial PDFs with weight factors depending on both the atomic concentrations and their neutron scattering lengths. The weighted sum was Fourier-transformed to obtain the total structure factor, which was Fourier-transformed again, with an experimentally consistent Q cutoff, to obtain the simulated PDFs.

https://doi.org/10.1021/acsaem.0c02678
ACS Appl. Energy Mater. 2021, 4, 3044−3056

Table 1. Normalized Weight Factors $w_{\alpha\beta}$

	Cl−Cl	Na−Cl	Cr−Cl	Na−Na	Na−Cr	Cr−Cr
neutron ^{53}Cr	0.771	0.317	−0.103	0.033	−0.021	0.0035
neutron ^{0}Cr	0.688	0.283	0	0.029	0	0
neutron ^{nat}Cr	0.626	0.258	0.073	0.026	0.015	0.0021
FOD	0	0	0.833	0	0.171	−0.0037
X-ray (at $Q = 0$)	0.149	0.356	0.118	0.212	0.141	0.024

consistency with which our ab-initio MD simulations predict PDFs for different isotopes of Cr means that the interatomic interactions are modeled correctly, especially the most important contributions from Cr−Cl and Cr−Na pairs. By utilizing a combination of neutron diffraction with isotopic substitution of ^{53}Cr, X-ray diffraction, and *ab initio* MD simulations, we demonstrate the formation of $CrCl_6^{3-}$ octahedra with Cr−Cl distances of 2.342 ± 0.003 Å and Cl−Cl distances of 3.50 ± 0.01 Å. The most likely distance between Cr^{3+} and Cl^- corresponds well with the sum of their Shannon radii (0.615 Å for Cr^{3+} and 1.81 Å for Cl^-).[34] As a result of the chromium−chloride attraction, Cl ions are on average closer together than they are in pure molten NaCl. On the other hand, the environment around Na ions is unaffected by Cr and it looks on average like it does in molten NaCl. We found the formation of chains and networks by corner- and edge-sharing octahedra. We also found evidence for a mid-range order that is likely related to interchain correlations. Therefore, our model ternary salt shows the structure that is reminiscent of NaCl−UCl_n,[35] the salt that is likely to be used in MSRs. We expect that Cr impurities will affect network formation of the abovementioned salts, thus affecting the diffusivity and viscosity, especially near salt−metal interfaces. Our results give us confidence that our model would correctly predict the effects of Cr impurities on the structure and physical properties of multicomponent salts.

3.1. Neutron Scattering. Measured neutron scattering intensity is proportional to the differential cross-section $d\sigma/d\Omega$, which itself is proportional to the total structure factor

$$S(Q) = \sum_{\alpha}\sum_{\beta} c_\alpha c_\beta b_\alpha b_\beta (S_{\alpha\beta}(Q) - 1) \tag{2}$$

where Q is the wavevector transfer, α and β represent salt components, c_α is the molar concentration of the α salt component, and b_α is the tabulated neutron scattering length of the component α. $S_{\alpha\beta}(Q)$ is the partial structure factor, which describes the structure of the melt. Thus, the result of the measurements is a weighted sum of six pairwise contributions, Cr−Cl, Cr−Na, Cr−Cr, Na−Cl, Cl−Cl, and Na−Na. Since the scattering length b_{Cr} is different for different Cr isotopes, isotopic substitutions can help us to determine $S_{\alpha\beta}(Q)$ by changing the coefficients $c_\alpha c_\beta b_\alpha b_\beta$ without changing the chemical composition of the samples. The scattering lengths of Cr are as follows: b_{Cr} = 3.635 fm for natural Cr (the mix of stable ^{50}Cr, ^{52}Cr, ^{53}Cr, and ^{54}Cr) and $b_{Cr_{53}}$ = −4.2 fm.[33] A mixture of natural ^{nat}Cr and ^{53}Cr was also made where b_{Cr_0} = 0, which is called zero-mix and denoted as ^{0}Cr. It is convenient to use dimensionless weight factors that are normalized such that $\sum_\alpha\sum_\beta c_\alpha c_\beta b_\alpha b_\beta = w_{\alpha\beta} = 1$. For the samples involved here, the weight factors are given in Table 1.

It is apparent from this table that the total neutron structure factor is dominated by the Cl−Cl partial due to the high concentration and the large coherent scattering length of chlorine. On the other hand, the contribution of the chromium partials is relatively small.

The pair distribution function (PDF) $g_n(r)$ is obtained through a discrete Fourier transform

$$r[g_n(r) - 1] = \frac{1}{2\pi^2\rho}\sum_{Q}^{Q_{max}} QS(Q)\sin(Qr)\Delta Q = r\sum_{\alpha\beta} w_{\alpha\beta}[g_{\alpha\beta}(r) - 1] \tag{3}$$

The physical meaning of a partial pair distribution function $g_{\alpha\beta}(r)$ is the probability of finding an atom at a distance r from another atom at the origin compared to the probability of finding an atom at the same distance in a completely disordered system. Figure 3 shows the measured and simulated total neutron PDFs.

To separate the contributions of Cr−Cl, Cr−Na, and Cr−Cr pairs, the normalized intensity of ^{53}Cr-substituted salt was subtracted from that of natural salt to obtain the first-order difference (FOD) differential cross-section per atom (fm^2/Sr/atom). To extract the PDF, we follow a well-established procedure.[19,37,38]

The difference between the signals from two isotopic compositions is that the FOD function contains only contributions from Cr−Cl, Cr−Na, and Cr−Cr pairs

$$\Delta S(Q) = S_{natural} - S_{isotopic} = w_{CrCl}[S_{CrCl}(Q) - 1] + w_{CrNa}[S_{CrNa}(Q) - 1] + w_{CrCr}[S_{CrCr}(Q) - 1] \tag{4}$$

where the values of the weight factors are listed in the FOD line of the Table 1: $w_{CrCl} = c_{Cr}c_{Cl}(b_{Cr} - b_{Cr_{53}})b_{Cl}$, $w_{CrNa} = c_{Cr}c_{Na}(b_{Cr} - b_{Cr_{53}})b_{Na}$, and $w_{CrCr} = c_{Cr}{}^2(b_{Cr}{}^2 - b_{Cr_{53}}{}^2)$.

As a result of eq 4, we can extract the contribution of only the pairs that contain Cr ions, namely, Cr−Cl, Cr−Na, and Cr−Cr (also, the instrumental background cancels, resulting in a high signal-to-background ratio). Figure 4 shows the FOD $\Delta g_n(r)$ for both

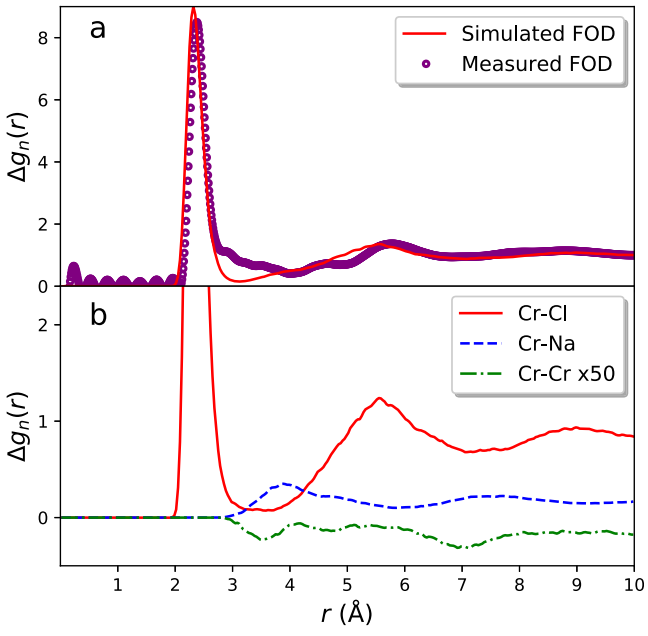

Figure 4. Measured and simulated FOD in the neutron pair distribution function ($\Delta g_n(r)$) for isotopically substituted NaCl−$^{53}CrCl_3$ and natural NaCl−$CrCl_3$. (a) Comparison between the measured (circles) and simulated (line) FOD. (b) Simulated partial PDFs that contribute to the FOD, Cr−Cl, Cr−Na, and Cr−Cr. The Cr−Cr contribution is very small; therefore, it is multiplied by a factor of 50 to show on the scale of the figure. The most likely nearest-neighbor and next-nearest-neighbor positions for the Cr−Cr pair can be identified as 3.5 and 7 Å, respectively.

https://doi.org/10.1021/acsaem.0c02678
ACS Appl. Energy Mater. 2021, 4, 3044−3056

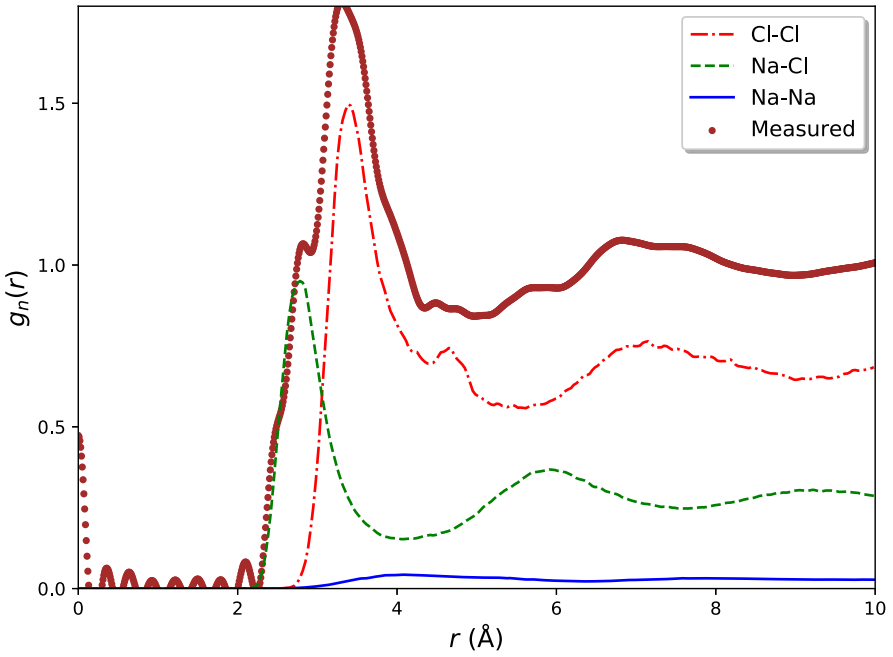

Figure 5. Measured and simulated PDFs (neutron) of the zero-mix NaCl−^{0}CrCl$_3$. The measured total PDF is denoted by brown dots, while simulated partials are as follows: blue line for Na−Na, green dashed line for Na−Cl, and red dash-dotted line for Cl−Cl.

measurements and simulations. The dominant sharp peak at 2.34 Å corresponds to the first shell of Cr−Cl neighbors, while the feature at ∼6 Å corresponds to the second Cr−Cl shell. The contribution from Cr−Cr pairs is very small due to the small weight factor $w_{CrCr} = -0.04$ fm^2 in eq 4. However, the first and second shells are visible at 3.5 and 7 Å, respectively.

The total structure factor is calculated from the measured intensities as follows

$$\left(\frac{d\sigma}{d\Omega}\right)_{FOD} = A\frac{I_{nat} - I_{53}}{I_v} \tag{5}$$

where I_{nat}, I_{53}, and I_v are the measured intensities of NaCl−CrCl$_3$, NaCl−^{53}CrCl$_3$, and vanadium calibration samples, respectively. A is related to the number of atoms in the beam and the incoherent vanadium cross-section

$$A = \frac{{d_v}^2\sigma_v\rho_v}{4\pi {d_s}^2\rho_s} = 156.3 \text{ fm}^2/\text{Sr} \tag{6}$$

where the subscript v stands for vanadium and s stands for sample.

Partial PDFs are determined as discrete Fourier transforms of the total structure factor

$$r[\Delta g_n(r) - 1] = \frac{1}{2\pi^2\rho}\sum_i Q\left[\left(\frac{\sigma}{d\Omega}\right)_{FOD} - P(Q)\right]\sin(Q_i r_j)\Delta Q \tag{7}$$

where $P(Q)$ is the Placzek correction.[37] The results are plotted in Figure 4, which shows that the first peak at 2.34 Å is due to Cr−Cl pairs only. Therefore, the integration of this peak was used to determine the coordination number (CN) $N(r_{max})$, namely, the number of Cl ions surrounding a Cr ion

$$N(r_{max}) = 4\pi c_{Cl}\rho\int_0^{r_{max}} \Delta g_n(r) r^2\, dr = 5.83 \tag{8}$$

where c_{Cl} is the atomic concentration of Cl (0.590), ρ is the total number density (0.0362 Å^{-3}), and r_{max} = 3.5 Å. We compared this experimental value of $N(r_{max})$ with AIMD simulations. The simulations resulted in N(3.2 Å) = 5.66 and N(3.7 Å) = 5.8, consistent with experiments and only weakly dependent on r_{max}.

To compare NaCl−CrCl$_3$ with NaCl, we use the zero-mix, which is a ^{53}Cr-enriched salt such that the neutron scattering length of Cr is zero, meaning that the Cr ions do not contribute to the measured diffraction signal (we denote such salt as NaCl−^{0}CrCl$_3$). The ratio of molar concentrations of natural Cr and ^{53}Cr corresponds to the ratio of coherent scattering lengths $b_{Cr} = 3.635$ fm and $b_{Cr_{53}} = -4.2$ fm. The zero-mix allows us to measure PDFs formed by pairs containing Na$^+$ and Cl$^-$ only and directly compare the structure with that of pure NaCl, which has been extensively studied. Figures 5 and 6 demonstrate this comparison. The strongest signals correspond to the first and second shells of Na−Cl and Cl−Cl pairs. The sum of the three simulated PDFs perfectly reproduces the measurements. Figure 6 shows simulated partial PDFs of Na- and Cl-containing pairs for NaCl−^{0}CrCl$_3$ and pure NaCl (from MD simulations based on a neural network interatomic potential[10]). Here, the partial $g_{\alpha\beta}(r)$ was calculated from AIMD trajectories according to the standard definition $g_{\alpha\beta}(r) = dn_{\alpha\beta}(r)/(4\pi r^2 dr\rho_\alpha)$, where $dn_{\alpha\beta}(r)$ is the number of α atoms around a given β atom at distances $r + dr$ and ρ_α is the average number density of α atoms in the entire sample. Remarkably, the distribution of Na−Cl and Na−Na distances is almost the same for both salts. The only difference is in Cl−Cl distribution, which shows the same features but smaller Cl−Cl distances due to the strong attraction from Cr^{3+} ions to form Cr^{3+}-centered octahedra (the most likely Cl−Cl vertex separation is ∼3.32 Å, as analyzed in the following). The comparison of the neutron partial structure factors of NaCl and NaCl−NaCrCl$_3$ is shown in Figure 7. Although the partial $S_n(Q)$ is reminiscent of each other, there are marked differences in the positions of the peaks.

Measurements of the static structure factor $S_n(Q)$ are shown in Figure 8. In addition to the expected short-range order, Figure 8 reveals a strong peak at ∼1 Å^{-1}. This peak is often referred to as the prepeak or the first sharp diffraction peak. Ab-initio simulations reproduce the short-range order very well (above 2 Å^{-1}), and they show features resembling the prepeak. It is not prominent in ab-initio simulations due to the small sample volume (the sample volume will be expanded once the simulations use neural network potentials, as demonstrated for a simpler NaCl melt[10]). Unlike NaCl−CrCl$_3$, where the prepeak is almost unchanged in the zero-mix, pure NaCl does not show the prepeak; see Figure 7. The comparison of the partial structure factors of NaCl and NaCl−CrCl$_3$ is shown in Figure 8.

https://doi.org/10.1021/acsaem.0c02678
ACS Appl. Energy Mater. 2021, 4, 3044−3056

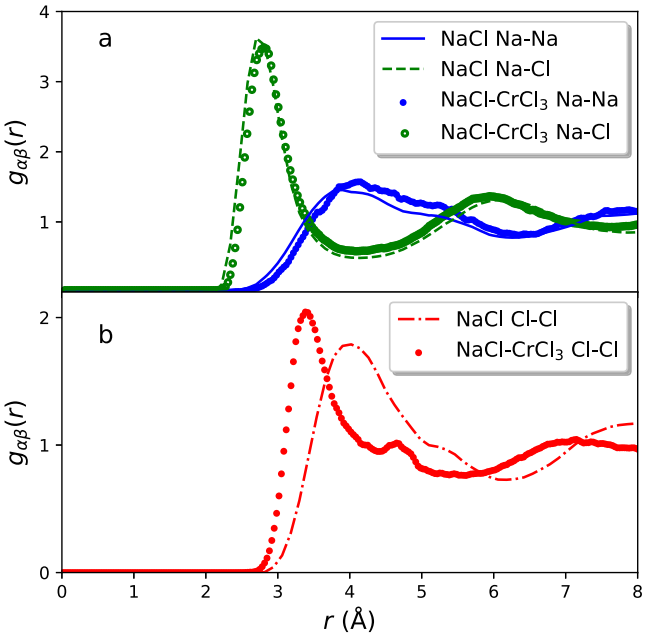

Figure 6. Simulated partial PDFs (neutron) of NaCl and zero-mix NaCl−$^{0}CrCl_3$. (a) Na−Na (blue line for NaCl and blue dots for NaCl−$^{0}CrCl_3$) and Na−Cl (green line for NaCl and green circles for NaCl−$^{0}CrCl_3$) and (b) Cl−Cl (red dash-dotted line for NaCl and red dots for NaCl−$^{0}CrCl_3$). These partial PDFs were directly obtained from the average structure in AIMD simulation (AIMD simulation details can be found in the Methods section).

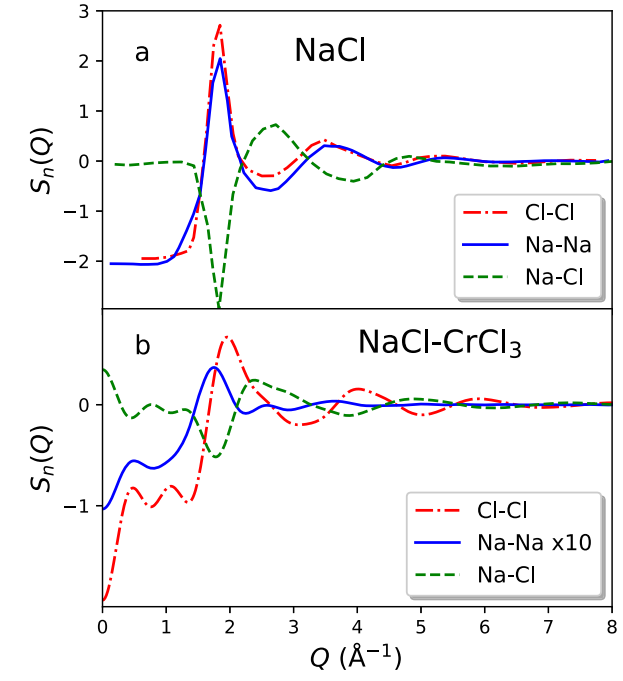

Figure 7. Comparison of the partial structure factors $S_n(Q)$ of NaCl and zero-mix NaCl−$CrCl_3$. (a) Partial structure factors of molten NaCl, as deduced by reverse Monte-Carlo from neutron diffraction measurements.[36] (b) Simulated partial $S(Q)$ that includes Cl−Cl, Na−Na, and Na−Cl pairs only.

To probe the nature of the prepeak, Figure 9 shows the FOD of the structure factor $\Delta S(Q)$ defined in eq 4. This figure shows that the prepeak is driven by correlations between Cr and Cl ions. The

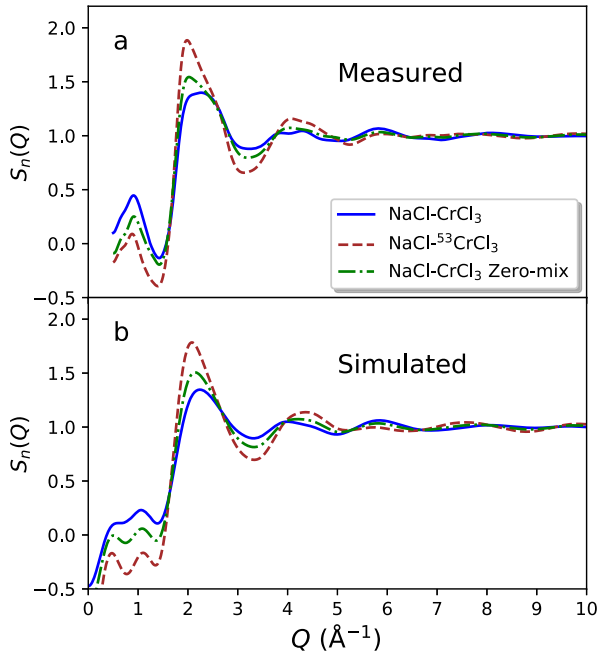

Figure 8. Structure factor (neutron) in molten NaCl−$CrCl_3$ at 700 °C. Three different isotopic compositions are shown for comparison. (a) Measured and (b) simulated.

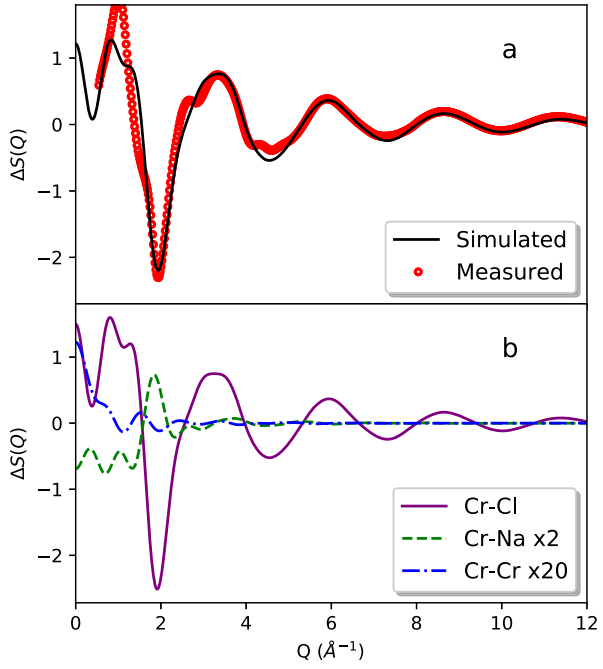

Figure 9. (a) Measured and simulated FOD in $S(Q)$ for isotopically substituted NaCl−$^{53}CrCl_3$ and natural NaCl−$CrCl_3$. (b) Simulated partial contributions to $\Delta S(Q)$. Note that the relatively small Cr−Na partial is multiplied by a factor of 2 and that of C−Cr is multiplied by 20 to show details.

prepeak corresponds to correlations that propagate over distances longer than nearest-neighbor distances.[3,39,40]

3.2. X-ray Scattering. Figure 10 shows the results of the $S_X(Q)$ measurements for NaCl−$CrCl_3$ at different temperatures. From this figure, we observe multiple regions with subtle differences in the structure. Below 485 °C, the $S_X(Q)$'s have intense peaks consistent with the crystalline state. The $S_X(Q)$ changes abruptly above 485 °C with the formation of some sharp diffraction peaks (related to large

https://doi.org/10.1021/acsaem.0c02678
ACS Appl. Energy Mater. 2021, 4, 3044−3056

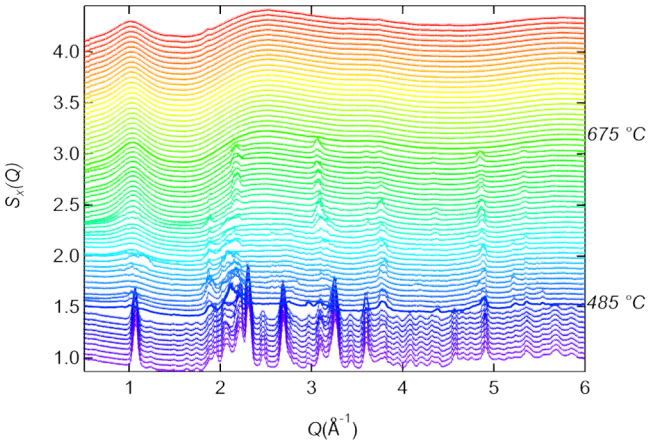

Figure 10. Structure factor $S_X(Q)$ (measured by X-rays) as a function of temperature for NaCl−$CrCl_3$. The 485 and 675 °C temperatures are highlighted as thicker traces and discussed within the text.

NaCl crystallites) superimposed on top of broad/diffuse peaks. This temperature corresponds to the melting T_m = 485 °C of the solid solution and is in general agreement with the results obtained using the temperature-scanning technique. At temperatures between 485 and 675 °C, the NaCl peaks decrease in intensity, with a concomitant increase in amplitude from the diffuse scattering component. Finally, above 675 °C, the $S_X(Q)$'s are composed of a single diffuse scattering component. Upon cooling, the transformation is reversible, with a reduction in the broad features and gradual emergence of sharp diffraction peaks. Another important observation from Figure 10 is the prepeak at ∼1 $Å^{-1}$. This peak in the liquid state corresponds to the so-called intermediate-range order.[39,41]

To follow the temperature evolution of the diffuse scattering in Figure 10, we refined the position, full width at half maximum (fwhm), and area of the prepeak (at ∼1.04 $Å^{-1}$) and the first diffraction peak (at ∼2.4 $Å^{-1}$) with a Gaussian and log−normal peak functions, respectively. The latter was needed due to the peak asymmetry. The fitting results for the two peaks are shown in Figure 11. Several temperature-dependent trends in the prepeak are observable from this figure, including an apparent inflection point at 575 °C and a clear reversal in trends for all refined parameters. The prepeak position changes slightly with temperature, while the width and area vary throughout the heating (and cooling) cycle. This is in contrast to the changes in the 2.4 $Å^{-1}$ peak, where above 575 °C, changes continue to appear linear.

The temperature dependence of the intermediate-range order, which manifests itself as the prepeak at 1 $Å^{-1}$ in the X-ray scattering results, has been studied before.[40,41] The position of the prepeak has been shown to evolve with temperature in either direction, increasing or decreasing in Q. In both cases, the most important influences are the decreasing density and increasing thermal motion with the temperature. In our case, we found that both the prepeak and the main diffraction peak that correspond to the Cr−Cl structure behave anomalously below about 600 °C, where the peaks move as if interionic distances decrease with increasing temperature. The temperature dependence of both 1 and 2.5 $Å^{-1}$ peaks above 575 °C is attributable to thermal expansion, which leads to a shift in the peak position, while thermal disorder leads to increased fwhm and a decrease in area. Note that the anomalies are all in the two-phase region and not in the single-phase liquid. In this region, we cannot exclude the effect of changing the concentration of species in the liquid as the solid NaCl dissolves with increasing temperature.

X-ray measured and simulated PDFs are shown in Figure 12 at different temperatures. With increasing temperature, Figure 12 shows changes in the pair correlations including a decrease in intensity associated with the Na−Cl and Na−Cr/Cr−Na correlation peaks at 2.65 and 4.0 Å, respectively.

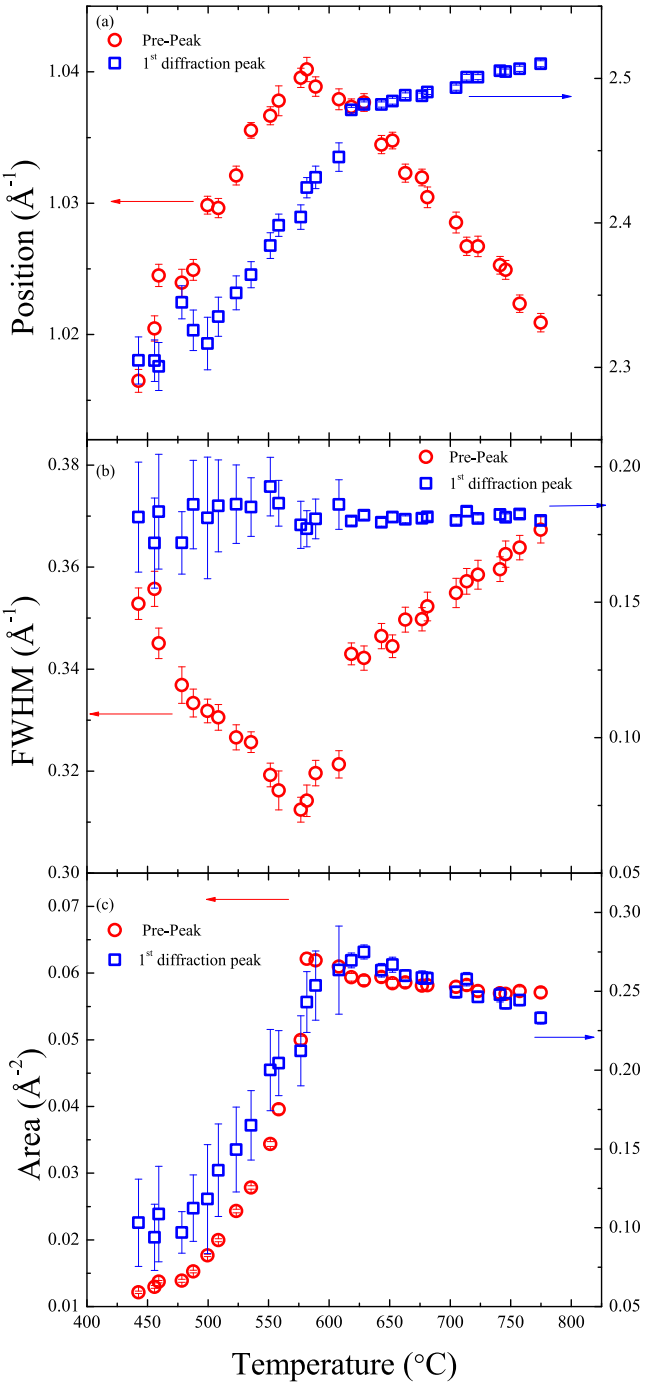

Figure 11. Temperature evolution of the position, fwhm, and area quantified the $S_X(Q)$ for the prepeak at ∼1 $Å^{-1}$ (red) and the first peak at ∼2.4 $Å^{-1}$ (blue).

We highlight the combination of neutron and X-ray diffraction measurements carried out in this work. These two probes complement each other to determine partial PDFs.[37,42] Neutrons are particularly useful for studying elements whose isotopes show relatively large differences in the neutron cross-section; examples include Cr, Ni, Li, and H among others. For instance, Figure 5 shows that Cl−Cl and Na−Cl make overwhelming contributions to the neutron signal except at the lowest r. The isotopic substitution of Cr allowed us to separate the signal from Cr, Na, and Cl, as shown in Figures 4 and 5. The significance of the isotopic substitution technique cannot be overestimated for studies of multicomponent melts. However, when isotopic substitution is not achievable (such as for Cs, F, and other elements that do not have stable isotopes with

https://doi.org/10.1021/acsaem.0c02678
ACS Appl. Energy Mater. 2021, 4, 3044−3056

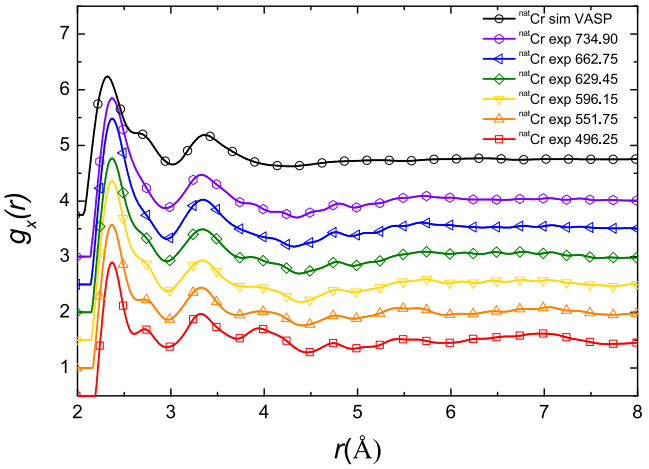

Figure 12. Pair distribution functions (X-ray) of molten NaCl−$CrCl_3$ measured and simulated. Measurements at different temperatures are shown, while simulations are at 700 °C. Note that the measurements below about 675 °C are in the two-phase state, where the relative concentration of Cr in the melt was likely changing with the temperature.

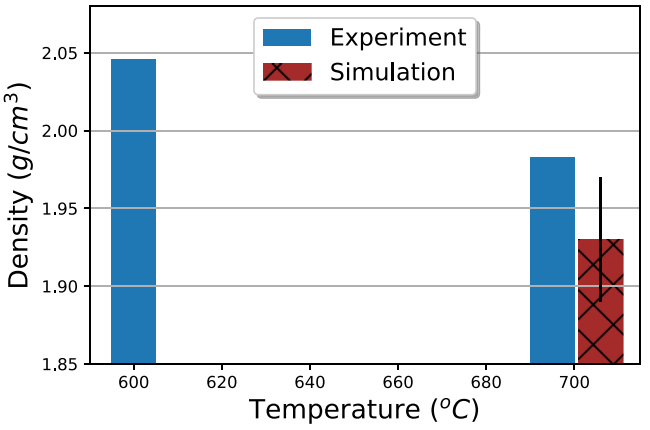

Figure 13. Density of molten NaCl−$CrCl_3$ at different temperatures. Solid (blue) bars are experimental measurements, while the hatched (brown) bar is the result of ab-initio simulations. The 600 °C point likely corresponds to the metastable two-phase mixture, so simulations were not done at this temperature. The error bar of the simulated density is shown. We estimate that the experimental error bars are smaller than those of the simulations based on very small errors in measurements of the length, angle, and weight.

large contrast for neutron diffraction), the combination of X-rays and neutrons can extract the information about partial PDFs not otherwise available. Equally importantly, neutrons and X-rays present very different experimental constraints such as compatibility between salts and crucibles, potential radiation damage to crucibles, and sometimes a large background from the crucibles and sample environment in general (*e.g.*, quartz crucibles are suitable for both neutrons and X-rays and can be used with chloride salts but not with fluoride salts). Our measurements demonstrate relative strengths and weaknesses of both techniques for studying the structure of multicomponent salts.

3.3. Density Measurements. We measured the density of molten NaCl−$CrCl_3$ by weighing the salt and measuring the volume of the melt. The volume was deduced from the height of the melt inside a calibrated crucible. The height was determined by inserting a 1 mm-diameter quartz rod into the molten salt at different temperatures. The molten salt visibly stained the quartz, and the stained part of the rod was used to determine the height. The error due to the displacement of the melt by the rod is extremely small because of its small volume. The rod's vertical orientation was the same for all measurements. The results are shown in Figure 13. The prediction from ab-initio molecular dynamics simulations is 1.93 g/cm^3 with a standard deviation of 0.04 g/cm^3, about three percent smaller than the measurement.

3.4. Melting Temperature. Temperature measurements on cooling (the cooling curve) showed the arrest point at about 454 °C.

NaCl−$CrCl_3$ salt in a glassy-carbon crucible was heated to 820 °C in a glovebox. The salt container was then removed from the furnace and the thermocouple was immediately inserted into the melt and the temperature was recorded till the salt naturally cooled down to about 150 °C. The arrest point was recorded, indicating a phase change at about 454 °C; see Figure 14.

This temperature corresponds well with X-ray diffraction results during both heating and cooling (Figure 10). The phase transition at 485 °C and the appearance of the liquid plus NaCl phase are at odds with the published phase diagram.[13] Importantly, our measurements of the structure were done at 700 °C with both neutrons and X-rays and are definitely in the liquid phase. The published phase diagram shows the formation of a congruently melting compound, Na_3CrCl_6, with the melting temperature of 620 °C. Our measurements, however, show a much lower melting point and the coexistence of NaCl crystals within the liquid between 485 and 675 °C. This low-temperature liquid is likely metastable due to a high potential barrier for the formation of Na_3CrCl_6 crystals, which contain multiple octahedra per unit cell. We postulate that the liquid persists to much lower

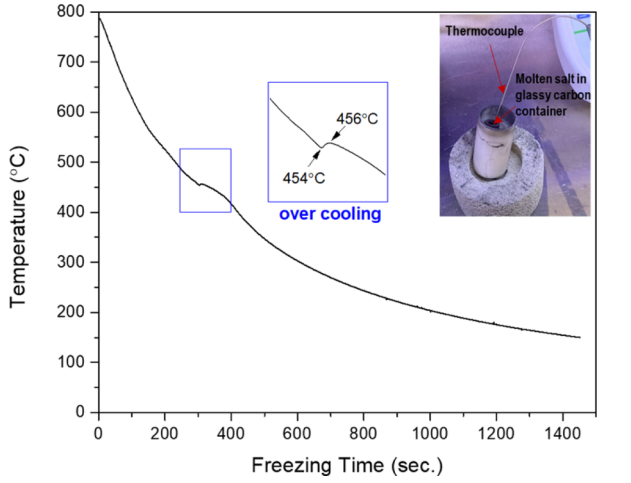

Figure 14. Temperature of NaCl−$CrCl_3$ as a function of time while naturally cooling in the glovebox. The inset in the upper-right corner shows the salt crucible and the thermocouple.

temperatures than expected due to a competition between the short-range order (networks of octahedra) and crystallization.

3.5. *Ab Initio* Molecular Dynamics Simulations. The simulations show the formation of $CrCl_6^{3-}$ octahedra, with bond angles of Cl−Cr−Cl triplets concentrated at ∼90 and ∼171°, while the Cl−Cl end-to-end distances clustered at ∼3.35 and ∼4.75 Å. $CrCl_6^{3-}$ octahedra are the dominant coordination environment with a fraction of at least 65%. The second dominant coordination environment is $CrCl_5^{2-}$, with a fraction between 20 and 32%. Figure 15 shows the distributions of the bond angles and end-to-end distances for Cl−Cr−Cl and Cr−Cl−Cr triplets. All configurations at T = 701.85 °C were used for such structural analyses (except for the first 4 ps ones that are considered equilibration steps), spanning a period of ∼35 ps. The statistics of Cl−Cr−Cl triplets provide local structural information around Cr^{3+} ions, while those of Cr−Cl−Cr triplets indicate how the octahedra connect to each other. Because of the relatively high concentration of Cr^{3+} ions in this eutectic system, $CrCl_6^{3-}$ octahedra are often interconnected to form chains or networks well beyond the first Cr−Cl shell. Octahedra can form corner-sharing, edge-sharing, and face-sharing connections.[43] Our simulations suggest

https://doi.org/10.1021/acsaem.0c02678
ACS Appl. Energy Mater. 2021, 4, 3044−3056

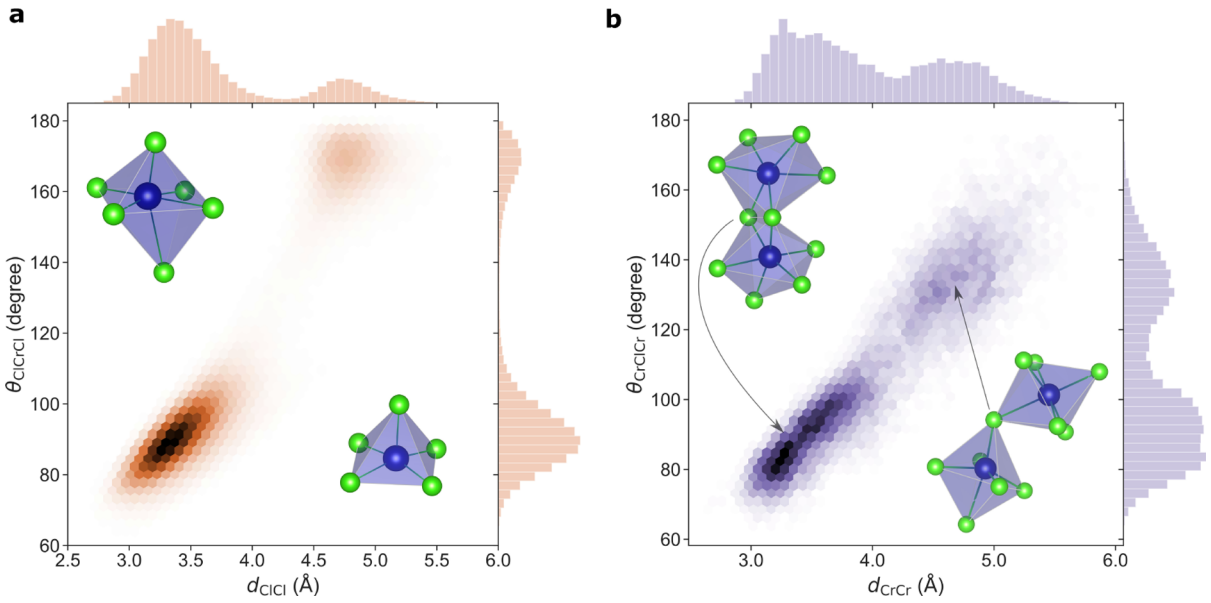

Figure 15. Parameters of Cr^{3+}-centered polyhedral structures from *ab initio* MD simulation. (a) Distributions of bond angles for Cl−Cr−Cl triplets and corresponding Cl−Cl distances, suggesting distorted Cr-centered octahedra (upper-left inset) or quadrilateral-based pyramids (lower-right inset). (b) Distributions of bond angles for Cr−Cl−Cr triplets and the corresponding Cr−Cr distances, suggesting dominant edge sharing (upper-left inset) and corner sharing (lower-right inset) among octahedra and pyramids. Color depths indicate the number of data points in each bin. The histograms along the abscissa and ordinate are sums of all bin values along the corresponding directions.

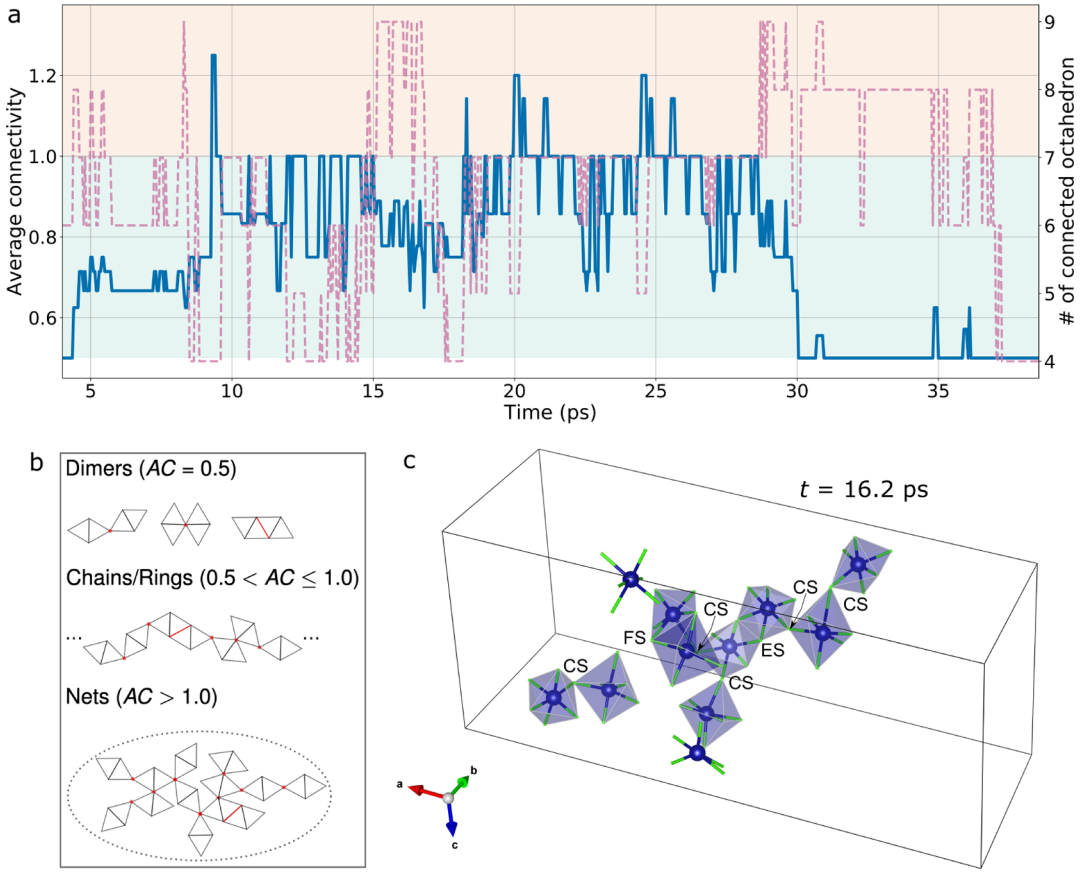

Figure 16. Connectivity evolution of Cr^{3+}-centered polyhedra from *ab initio* MD simulations. (a) Evolution of average connectivity (AC, solid line; see text for definition) among polyhedra and the number of connected polyhedra (dashed line). (b) Schematic illustration of different polyhedral connections and the corresponding values of AC. (c) Snapshot at t = 16.2 ps showing connections for nine octahedra. The AC for this configuration is 0.89 and the majority of them connect each other in the form of chains (although a local net and a dimer are also present). Corner sharing, edge sharing, and face sharing between octahedra are labeled as CS, ES, and FS, respectively. Na^+ and Cl^- ions are not displayed for clarity.

https://doi.org/10.1021/acsaem.0c02678
ACS Appl. Energy Mater. 2021, 4, 3044−3056

that corner sharing and edge sharing are the dominant connections in our system.

Next, we analyze how the connectivity among octahedra evolves with time. To this end, we identified and counted corner-sharing, edge-sharing, face-sharing, and isolated octahedra in each configuration. For each Cr^{3+} ion, we employed a cutoff distance of d_{CrCr} = 5.75 Å to identify its neighboring Cr^{3+} ions; see Figure 15. If a Cr^{3+} ion does not have any neighboring Cr^{3+} ions or if it does not share any Cl^- ions with its neighboring Cr^{3+} ions, then, we identify it as an isolated octahedron. If one Cl^- ion is shared between two neighboring Cr^{3+} ions, we count this as one corner sharing. Similarly, if two or three Cl^- ions are shared between two neighboring Cr^{3+} ions, we count it as one edge or face sharing. The cutoff distance to identify shared Cl^- ions is d_{CrCl} = 3.2 Å, a value near the first minimum on the Cr−Cl PDF. With these counts, we define a parameter called as the average connectivity (AC), which characterizes the extent of octahedral connection in a given configuration

$$\mathrm{AC} \equiv \frac{N_{CS} + N_{ES} + N_{FS}}{N_{total}^{Cr} - N_{isolated}^{Cr}} \tag{9}$$

where N_{CS}, N_{ES}, and N_{FS} are the number of corner-sharing, edge-sharing, and face-sharing octahedra, respectively. N_{total}^{Cr} is the total number of Cr^{3+} ions, while $N_{isolated}^{Cr}$ is the number of isolated Cr^{3+} ions. AC defined in eq 9 is the average number of connections per *connected* octahedron, similar to the average number of bonds per atom in a crystal. Figure 16 shows the time evolution of AC (solid line) and the number of connected octahedra (dashed line). To understand the physical meaning of such an evolution, we divided AC into different regimes. As shown in Figure 16b, if octahedra form a dimer, then AC = 0.5. For chains or rings, the average connections per octahedron are between 0.5 and 1.0, depending on the length of the chain. AC > 1.0 means that each octahedron on average has at least three connections, thus suggesting the formation of networks. Based on this understanding, we divided the plot in Figure 16a into two regions; the light-blue-shaded region contains chains of rings of connected octahedra, while the light-yellow region contains networks. The lowest value AC = 0.5 simply means that all connected octahedra are in the form of dimers. As can be seen, there are six connected octahedra at the beginning of this plot, but all of them exist as dimers, that is, three dimers in total. As the simulation continues, the connected octahedra fluctuate between 4 and 9, presenting chains or rings and occasionally forming networks until reaching the point of 30 ps. After that, the chains/rings are broken down and most of the octahedra form dimers or very short chains, suggesting that the lifetime of such chains/rings is in the order of 10 ps. Figure 16c shows a snapshot at t = 16.2 ps, where there are nine connected octahedra, consistent with the plot in Figure 16a. As can be seen, seven of the connected octahedra form a chain and two of them form a dimer. The connections of this chain consist of corner sharing, edge sharing, and face sharing, demonstrating excellent consistency with the AC = 0.89 in Figure 16a. From this analysis, we can see that Cr^{3+}-centered octahedra are an essential structural motif in this system, and they often interconnect to form chains/rings or even networks with a lifetime in the order of 10 ps. Previous studies suggested that correlations between neighboring chains of octahedra are the reason behind the prepeak at about 1 $Å^{-1}$.[39] Since only a single chain or isolated dimers were observed throughout current AIMD simulations, we expect that a larger simulation box would be required to observe interchain correlations and thus the prepeak.

Our simulations suggest that corner sharing and edge sharing are the dominant connections in our system. As seen in Figure 15a, bond angles of Cl−Cr−Cl triplets concentrate at ∼90 and ∼171°, while the Cl−Cl end-to-end distances cluster at ∼3.35 and ∼4.75 Å. Such geometrical relations suggest the formation of Cr^{3+}-centered octahedra or pyramids, as shown in the insets of Figure 15a. For regular octahedra, the shorter Cl−Cl distance is $\sqrt{2}$ times the Cr−Cl distance, while the longer Cl−Cl end-to-end distance is twice the Cr−Cl distance. In comparison, our *ab initio* MD results suggest factors of 1.425 (3.35/2.35) and 2.02 (4.75/2.35), , consistent with the octahedral structural motif. Due to large thermal fluctuations at T = 701.85 °C, most octahedra are highly distorted; thus, both bond angles and Cl−Cl distances show wide variations in their values. As shown in Figure 15b, the distribution of bond angles and Cr−Cr distances for Cr−Cl−Cr triplets shows two dominant clusters. The lower-left cluster is centered at the bond angle around 90° with a corresponding Cr−Cr distance near 3.44 Å. This observation is consistent with the scenario of edge sharing between two regular octahedra, where the bond angle for Cr−Cl−Cr triplets is 90° and the corresponding Cr−Cr distance is 3.32 Å. We note that the observed Cr−Cr distance is on average slightly larger than that derived from two regular edge-sharing octahedra. This difference could be ascribed to the repulsive interactions between Cr^{3+} ions (ignored in the calculation using two regular octahedra). On the other hand, another cluster in Figure 15b is centered at a bond angle of ∼133° and a Cr−Cr distance of ∼4.65 Å that correspond to corner-sharing octahedra with certain folding between two Cr−Cl bonds. Such folding can be due to the attraction between Cr^{3+} and Cl^- ions from neighboring octahedra. The configuration where Cr−Cl−Cr triplets form a straight line (*i.e.*, the bond angle of 180°) should be an unstable (or shallow metastable) state such that thermal fluctuations may easily break the subtle equilibrium and cause the system to fall into the more stable folding configuration. The bond angle in this local minimum is mainly determined by the attractions between Cr^{3+} and Cl^- ions, the repulsion between Cr^{3+} ions, and the repulsion between Cl^- ions. The average Cr−Cr distance is also larger than that from the ideal case with a bond angle of 133° (4.31 Å) due to the repulsive interactions between Cr^{3+} ions.

4. DISCUSSION AND CONCLUSIONS

To illustrate the level of insight that our studies offer into the structure of molten NaCl−$CrCl_3$, we synthesize the findings by simulations and experiments. Although the formation of octahedra and their chains is not unexpected for Cr^{3+} ions in NaCl, they have been studied here for the first time. At the same time, we showed that partial PDFs in the Na−Cl subsystem are unaffected by the presence of Cr; see Figure 6 a. In Figure 6 b, note the characteristic small peak at ∼4.8 Å. This separation corresponds to the distance between two opposite vertices of the octahedra. We found that in pure NaCl, the most popular coordination number is 6, which should correspond to an octahedral local structure, considering that Cl−Na−Cl angles are mostly 90°.[10] Considering that the most likely Na−Cl distance is ∼2.76 Å, the most likely separation between two opposite vertices of octahedra will be 5.52 Å. This number matches well with the observed secondary peak at ∼5.5 Å in the Cl−Cl partial PDF of NaCl−$CrCl_3$ that appears also in NaCl at ∼5.5 Å. It is worth noting that such a detailed insight into the structure of the Cr-containing melt is made possible by the availability of different Cr isotopes with both positive and negative neutron scattering lengths, thus making isotopic substitution a very effective tool for probing the structure of the liquid. Given the common structural motifs between Cr and other multivalent cations (especially transition metals but also rare earths and actinides), Cr could serve as a model ion to experimentally probe some of the structures and dynamics with high resolution.

There are multiple implications of our findings for molten-salt reactors (MSRs). The motivation of this work is to provide structural information that can be utilized as experimental validation for developing novel atomistic models such as neural network interatomic potentials.[9,10,44] The need for such simulations stems from the need to predict physical properties of molten salts such as density, heat capacity, viscosity, and so on. It is impractical to measure all these properties and their

https://doi.org/10.1021/acsaem.0c02678
ACS Appl. Energy Mater. 2021, 4, 3044−3056

changes for many different salt compositions especially when the melts could contain more than 10 components and impurities. However, computer simulations can predict these properties well if the interatomic potentials are known.[6,45] As the first step, we demonstrated a remarkable overall agreement between our *ab initio* MD simulations and measurements of Cr-containing molten salts.

Although Cr impurities in real systems will be at a very low level, by studying high Cr concentration here, we were able to validate computer simulations with high fidelity. Cr-ion concentration will be the highest near surfaces, where the impurity will affect the diffusivity, viscosity, and redox potential of the salt, thus affecting the corrosion rate directly. The interaction between corrosion products with dissolved nuclear fuel and other salt components needs to be predicted based on models such as that successfully tested here.[7] Importantly, $Cr-Cl_6$ octahedra are very similar to $U-Cl_6$ octahedra in U-containing salts. Indeed, let us compare the octahedra formed in molten $NaCl-CrCl_3$ and $NaCl-UCl_3$ (78 mol % NaCl). In the uranium salt, the most likely distance between U^{3+} and Cl^- is 2.74 Å.[35] This is larger than the Cr−Cl distance of 2.342 Å, as dictated by the larger Shannon radius of U^{3+} (1.025 Å for U^{3+} *vs* 0.615 Å for Cr^{3+}).[34] Also, the coordination numbers of the metal ions are the same in both salts at similar concentrations, CN ≈ 5.8. The difference between the salts is in the connectivity between octahedra; see Figure 16. While the Cr ions tend to form multiple-octahedral chains, the corresponding U salt has only 10% octahedra in trimers and 20% in dimers, while the vast majority are monomers. Therefore, it is conceivable that the presence of Cr ions in U salts could modify the structure and thus affect macroscopic physical properties.

The unexpected observation of the supercooled liquid and NaCl precipitation is important because the molten-salt chemistry in MSRs is normally approached within a chemical−thermodynamic equilibrium framework, assuming that chemical reactions and phase transitions are very rapid at reactor operating temperatures, up to 650 °C. However, this assumption may not be valid in a dynamic system such as an MSR. For instance, the fuel salt is going to experience temperature transients of about 100 °C within minutes as it circulates through the system, potentially leading to the formation of precipitates and out-of-equilibrium phases. Examples of non-equilibrium effects have previously been observed in molten-salt systems such as the formation of complex ions and changes in ion coordination may have caused a melting point depression in NH_4NO_3 salts with added metals (Li, Na, K, Ag, Ca, Sr, and Pb).[46] Also, compound formation in a $LiCl-Li_2O$ salt used in the production of uranium metal caused lowering of the melting point and covaporization of the $LiCl-Li_2O$ salt.[47] However, a detailed analysis of non-equilibrium effects has not yet been done for molten-salt systems relevant to MSRs, where nuclear reactions produce heat in circulating melts.[48] The idealized two-component salt studied here can be used to approach this problem since observations have shown a supercooled liquid 200 °C below the published equilibrium melting. Specifically, we have observed a supercooled liquid, where the intermediate-range order is stabilized with increasing temperature until the equilibrium melting temperature is reached.[49,50] Such results are important for approaching the non-equilibrium phenomena arising due to temperature cycling relevant to operating MSRs.

AUTHOR INFORMATION

Corresponding Authors

Ju Li − *Department of Nuclear Science and Engineering and Department of Materials Science and Engineering, Massachusetts Institute of Technology, Cambridge, Massachusetts 02139, United States;* orcid.org/0000-0002-7841-8058; Email: liju@mit.edu

Boris Khaykovich − *Nuclear Reactor Laboratory, Massachusetts Institute of Technology, Cambridge, Massachusetts 02139, United States;* orcid.org/0000-0002-9490-2771; Email: bkh@mit.edu

Authors

Qing-Jie Li − *Department of Nuclear Science and Engineering, Massachusetts Institute of Technology, Cambridge, Massachusetts 02139, United States*

David Sprouster − *Department of Materials Science and Chemical Engineering, Stony Brook University, Stony Brook, New York 11784, United States;* orcid.org/0000-0002-2689-0721

Guiqiu Zheng − *Nuclear Reactor Laboratory, Massachusetts Institute of Technology, Cambridge, Massachusetts 02139, United States*

Jörg C. Neuefeind − *Neutron Scattering Science Directorate, Oak Ridge National Laboratory, Oak Ridge, Tennessee 37831-6475, United States*

Alexander D. Braatz − *Isotopes and Fuel Cycle Technology Division, Oak Ridge National Laboratory, Oak Ridge, Tennessee 37831-6243, United States*

Joanna Mcfarlane − *Isotopes and Fuel Cycle Technology Division, Oak Ridge National Laboratory, Oak Ridge, Tennessee 37831-6243, United States;* orcid.org/0000-0002-4112-5104

Daniel Olds − *National Synchrotron Light Source II, Brookhaven National Laboratory, Upton, New York 11973, United States*

Stephen Lam − *Department of Nuclear Science and Engineering, Massachusetts Institute of Technology, Cambridge, Massachusetts 02139, United States; Department of Chemical Engineering, University of Massachusetts Lowell, Lowell, Massachusetts 01854, United States;* orcid.org/0000-0002-7683-1201

Complete contact information is available at: https://pubs.acs.org/10.1021/acsaem.0c02678

Notes

The authors declare no competing financial interest.

ACKNOWLEDGMENTS

We acknowledge multiple useful discussions with Richard Mayes, Stephen Raiman, Jake McMurray (ORNL), and Raluca Scarlat (UC Berkeley). We acknowledge the help of Abbey McAllister (ORNL) with sample handling and preparation. This material is based upon work supported by the Department of Energy under Award Number DE-NE0008751. This research used resources at the Spallation Neutron Source, a U.S. Department of Energy (DOE) Office of Science User Facility operated by the Oak Ridge National Laboratory, and the beamline 28-ID-1 (PDF) of the National Synchrotron Light Source II, a DOE Office of Science User Facility operated for the DOE Office of Science by Brookhaven National Laboratory under contract no. DE-SC0012704. This

https://doi.org/10.1021/acsaem.0c02678
ACS Appl. Energy Mater. 2021, 4, 3044−3056

work also used the Extreme Science and Engineering Discovery Environment (XSEDE) resources at the Texas Advanced Computing Center (TACC) through allocation DMR190055.

REFERENCES

(1) Williams, D. F.; Britt, P. F. *Technology and Applied R&D Needs for Molten Salt Chemistry*; Report for the US Department of Energy, Office of Nuclear Energy, 2017.
(2) Lantelme, F.; Groult, H. *Molten Salts Chemistry: From Lab to Applications*; Newnes, 2013.
(3) Rollet, A.-L.; Salanne, M. Studies of the local structures of molten metal halides. *Annu. Rep. Prog. Chem., Sect. C: Phys. Chem.* **2011**, *107*, 88−123.
(4) Hansen, J.-P.; McDonald, I. R. *Theory of Simple Liquids: With Applications to Soft Matter*; Academic Press, 2013.
(5) Egelstaff, P. *An Introduction to the Liquid State*; Elsevier, 2012.
(6) Gheribi, A. E.; Corradini, D.; Dewan, L.; Chartrand, P.; Simon, C.; Madden, P. A.; Salanne, M. Prediction of the thermophysical properties of molten salt fast reactor fuel from first-principles. *Mol. Phys.* **2014**, *112*, 1305−1312.
(7) Nam, H. O.; Bengtson, A.; Vörtler, K.; Saha, S.; Sakidja, R.; Morgan, D. First-principles molecular dynamics modeling of the molten fluoride salt with Cr solute. *J. Nucl. Mater.* **2014**, *449*, 148−157.
(8) Liu, M.; Masset, P.; Gray-Weale, A. Solubility of Sodium in Sodium Chloride: A Density Functional Theory Molecular Dynamics Study. *J. Electrochem. Soc.* **2014**, *161*, E3042−E3048.
(9) Behler, J.; Parrinello, M. Generalized neural-network representation of high-dimensional potential-energy surfaces. *Phys. Rev. Lett.* **2007**, *98*, 146401.
(10) Li, Q.-J.; Kucukbenli, E.; Lam, S.; Khaykovich, B.; Kaxiras, E.; Li, J. Development of robust neural-network interatomic potential for molten salt: an application to molten NaCl. *Cell Rep. Phys. Sci.* **2021**, 100359.
(11) Raiman, S. S.; Lee, S. Aggregation and data analysis of corrosion studies in molten chloride and fluoride salts. *J. Nucl. Mater.* **2018**, *511*, 523−535.
(12) Korshunov, B. G.; Raskin, B. Y. *Zh. Neorg. Khim.* **1962**, *7*, 1137−1140.
(13) Cook, C. M., Jr The systems NaCl—CrCl3 and KCl—CrCl3. *J. Inorg. Nucl. Chem.* **1963**, *25*, 123−127.
(14) Vasil'kova, I. V.; Efimov, A. I.; Pitirimov, B. Z. Complex formation in the MCl-CrCl3 system (M = alkali metals). *Zh. Neorg. Khim.* **1964**, *9*, 900−904.
(15) Oki, T.; Tanikawa, J. Equilibrium phase diagrams of the CrCl3-NaCl and CrCl3-KCl systems. *Denki Kagaku* **1968**, *36*, 119−123.
(16) *Phase Equilibria Diagrams Online Database (NIST Standard Reference Database 31)*, 2021, www.nist.gov/srd/nist31.cfm.
(17) Shaffer, J. H. *Preparation and Handling of Salt Mixtures for the Molten Salt Reactor Experiment*; Oak Ridge National Lab., 1971.
(18) Thoma, R. E. *Chemical Aspects of MSRE Operations*; Oak Ridge National Lab., 1971.
(19) Neuefeind, J.; Feygenson, M.; Carruth, J.; Hoffmann, R.; Chipley, K. K. The Nanoscale Ordered Materials Diffractometer NOMAD at the Spallation Neutron Source SNS. *Nucl. Instrum. Methods Phys. Res., Sect. B* **2012**, *287*, 68−75.
(20) Egami, T.; Billinge, S. J. *Underneath the Bragg Peaks: Structural Analysis of Complex Materials*; Newnes, 2012.
(21) Juhás, P.; Davis, T.; Farrow, C. L.; Billinge, S. J. L. PDFgetX3: a rapid and highly automatable program for processing powder diffraction data into total scattering pair distribution functions. *J. Appl. Crystallogr.* **2013**, *46*, 560−566.
(22) Kresse, G.; Hafner, J. Ab initiomolecular dynamics for liquid metals. *Phys. Rev. B: Condens. Matter Mater. Phys.* **1993**, *47*, 558−561.
(23) Kresse, G.; Hafner, J. Ab initiomolecular-dynamics simulation of the liquid-metal-amorphous-semiconductor transition in germanium. *Phys. Rev. B: Condens. Matter Mater. Phys.* **1994**, *49*, 14251−14269.
(24) Kresse, G.; Furthmüller, J. Efficient iterative schemes forab initiototal-energy calculations using a plane-wave basis set. *Phys. Rev. B: Condens. Matter Mater. Phys.* **1996**, *54*, 11169−11186.
(25) Kresse, G.; Furthmüller, J. Efficiency of ab-initio total energy calculations for metals and semiconductors using a plane-wave basis set. *Comput. Mater. Sci.* **1996**, *6*, 15−50.
(26) Perdew, J. P.; Burke, K.; Ernzerhof, M. Generalized Gradient Approximation Made Simple. *Phys. Rev. Lett.* **1996**, *77*, 3865−3868.
(27) Perdew, J. P.; Burke, K.; Ernzerhof, M. Generalized Gradient Approximation Made Simple [Phys. Rev. Lett. 77, 3865 (1996)]. *Phys. Rev. Lett.* **1997**, *78*, 1396.
(28) Blöchl, P. E. Projector augmented-wave method. *Phys. Rev. B: Condens. Matter Mater. Phys.* **1994**, *50*, 17953−17979.
(29) Kresse, G.; Joubert, D. From ultrasoft pseudopotentials to the projector augmented-wave method. *Phys. Rev. B: Condens. Matter Mater. Phys.* **1999**, *59*, 1758−1775.
(30) Grimme, S. Semiempirical GGA-type density functional constructed with a long-range dispersion correction. *J. Comput. Chem.* **2006**, *27*, 1787−1799.
(31) Martínez, L.; Andrade, R.; Birgin, E. G.; Martínez, J. M. PACKMOL: A package for building initial configurations for molecular dynamics simulations. *J. Comput. Chem.* **2009**, *30*, 2157−2164.
(32) Bengtson, A.; Nam, H. O.; Saha, S.; Sakidja, R.; Morgan, D. First-principles molecular dynamics modeling of the LiCl-KCl molten salt system. *Comput. Mater. Sci.* **2014**, *83*, 362−370.
(33) Koester, L.; Knopf, K.; Waschkowski, W. Interactions of slow neutrons with the chromium isotopes. *Z. Phys. A: At. Nucl.* **1978**, *287*, 61−69.
(34) Shannon, R. D. Revised effective ionic radii and systematic studies of interatomic distances in halides and chalcogenides. *Acta Crystallogr., Sect. A: Cryst. Phys., Diffr., Theor. Gen. Crystallogr.* **1976**, *32*, 751−767.
(35) Li, B.; Dai, S.; Jiang, D.-e. First-Principles Molecular Dynamics Simulations of UCln-NaCl (n = 3, 4) Molten Salts. *ACS Appl. Energy Mater.* **2019**, *2*, 2122−2128.
(36) Biggin, S.; Enderby, J. E. Comments on the structure of molten salts. *J. Phys. C: Solid State Phys.* **1982**, *15*, L305.
(37) Fischer, H. E.; Barnes, A. C.; Salmon, P. S. Neutron and x-ray diffraction studies of liquids and glasses. *Rep. Prog. Phys.* **2005**, *69*, 233.
(38) Skinner, L. B.; Benmore, C. J.; Weber, J. K. R.; Tumber, S.; Lazareva, L.; Neuefeind, J.; Santodonato, L.; Du, J.; Parise, J. B. Structure of Molten CaSiO3: Neutron Diffraction Isotope Substitution with Aerodynamic Levitation and Molecular Dynamics Study. *J. Phys. Chem. B* **2012**, *116*, 13439−13447.
(39) Wu, F.; et al. Elucidating Ionic Correlations Beyond Simple Charge Alternation in Molten MgCl2-KCl Mixtures. *J. Phys. Chem. Lett.* **2019**, *10*, 7603−7610.
(40) Iyetomi, H.; Vashishta, P.; Kalia, R. K. Integral-equation approach to medium-range order in molten and glassy chalcogenides. *Phys. Rev. B: Condens. Matter Mater. Phys.* **1991**, *43*, 1726.
(41) Wu, F.; Sharma, S.; Roy, S.; Halstenberg, P.; Gallington, L. C.; Mahurin, S. M.; Dai, S.; Bryantsev, V. S.; Ivanov, A. S.; Margulis, C. J. Temperature Dependence of Short and Intermediate Range Order in Molten $MgCl_2$ and its Mixture with KCl. *J. Phys. Chem. B* **2020**, *124*, 2892.
(42) Zeidler, A.; Salmon, P. S.; Martin, R. A.; Usuki, T.; Mason, P. E.; Cuello, G. J.; Kohara, S.; Fischer, H. E. Structure of liquid and glassy $ZnCl_2$. *Phys. Rev. B: Condens. Matter Mater. Phys.* **2010**, *82*, 104208.
(43) Wells, A. F. The octahedron in chemistry. *J. Solid State Chem.* **1973**, *6*, 469−478.
(44) Takamoto, S.; Izumi, S.; Li, J. TeaNet: universal neural network interatomic potential inspired by iterative electronic relaxations. **2019**, arXiv:1912.01398. arXiv preprint.

https://doi.org/10.1021/acsaem.0c02678
ACS Appl. Energy Mater. 2021, 4, 3044−3056

(45) Corradini, D.; Madden, P. A.; Salanne, M. Coordination numbers and physical properties in molten salts and their mixtures. *Faraday Discuss.* **2016**, *190*, 471−486.
(46) Shirai, T. Some physico-chemical properties of molten Ammonium nitrate. *Scientific Papers of the College of General Education*; University of Tokyo, 1960; p 10.
(47) Hur, J. M.; Park, S. B.; Seo, C. S.; Jung, K. J.; Park, S. W. Melting and vaporization of salts in a U-LiCl-Li2O system. *J. Radioanal. Nucl. Chem.* **2006**, *270*, 489−493.
(48) Nicolino, C.; Lapenta, G.; Dulla, S.; Ravetto, P. Coupled dynamics in the physics of molten salt reactors. *Ann. Nucl. Energy* **2008**, *35*, 314−322.
(49) Crichton, W. A.; Mezouar, M.; Grande, T.; Stølen, S.; Grzechnik, A. Breakdown of intermediate-range order in liquid GeSe2 at high pressure. *Nature* **2001**, *414*, 622−625.
(50) Salmon, P. S.; Martin, R. A.; Mason, P. E.; Cuello, G. J. Topological versus chemical ordering in network glasses at intermediate and extended length scales. *Nature* **2005**, *435*, 75−78.

https://doi.org/10.1021/acsaem.0c02678
ACS Appl. Energy Mater. 2021, 4, 3044−3056